The influence of helium-induced defects on the migration of strontium implanted into SiC above critical amorphization temperature

T. F. Mokgadi[1]*, Z. A. Y. Abdalla[1], M. Madhuku[2], E. G. Njoroge[1], M. Mlambo[3], P. Mdluli[3], A. Sohatsky[4], V. A. Skuratov[4,5,6], J. B. Malherbe[1] and T. T. Hlatshwayo[1]*

[1]Physics Department, University of Pretoria, Hatfield, South Africa, [2]iThemba LABS TAMS, National Research Foundation, Johannesburg, South Africa, [3]Nanotechnology Innovation Centre, Health Platform, Advanced Materials Division, Mintek, Randburg, South Africa, [4]Joint Institute for Nuclear Research, Dubna, Russia, [5]Moscow Engineering Physics Institute (MEPhI), National Research Nuclear University, Moscow, Russia, [6]Department of Nuclear Physics, Dubna State University, Dubna, Russia

The presence of radiation-induced defects and the high temperature of implantation are breeding grounds for helium (He) to accumulate and form He-induced defects (bubbles, blisters, craters, and cavities) in silicon carbide (SiC). In this work, the influence of He-induced defects on the migration of strontium (Sr) implanted into SiC was investigated. Sr-ions of 360 keV were implanted into polycrystalline SiC to a fluence of 2×10^{16} Sr-ions/cm^2 at 600°C (Sr-SiC). Some of the Sr-SiC samples were then co-implanted with He-ions of 21.5 keV to a fluence of 1×10^{17} He-ions/cm^2 at 350°C (Sr + He-SiC). The Sr-SiC and Sr + He-SiC samples were annealed for 5 h at 1,000°C. The as-implanted and annealed samples were characterized by Raman spectroscopy, scanning electron microscopy (SEM), atomic force microscopy (AFM), transmission electron microscopy (TEM), and Rutherford backscattered spectrometry (RBS). Implantation of Sr retained some defects in SiC, while co-implantation of He resulted in the formation of He-bubbles, blisters, and craters (exfoliated blisters). Blisters close to the critical height and size were the first to exfoliate after annealing. He-bubbles grew larger after annealing owing to the capture of more vacancies. In the co-implanted samples, Sr was located in three regions: the crystalline region (near the surface), the bubble region (where the projected range of Sr was located), and the damage region toward the bulk. Annealing the Sr + He-SiC caused the migration of Sr towards the bulk, while no migration was observed in the Sr-SiC samples. The migration was governed by "vacancy migration driven by strain fileds."

1 Introduction

Owing to its impeccable properties, viz., its creep and oxidation resistance (Carter et al., 1984; Pint et al., 2013; Avincola et al., 2015), radiation tolerance (Katoh et al., 2004; Katoh et al., 2007; Snead et al., 2007; Snead et al., 2011), low neutron capture cross-section (George et al., 2015), low radioactivity (Butterworth, 1989), and perfect chemical stability (Terrani

et al., 2014), silicon carbide (SiC) is used as a primary coating layer for retention of non-gaseous fission products in a self-containing modern high-temperature reactor fuel—the tri-structural isotropic (TRISO) coated fuel particle. The fuel is enclosed by chemical vapour deposited (CVD) layers that serve as barriers to the release of fission products. At the center of the TRISO particle is the fuel kernel (UO_2), which is surrounded by four layers in succession. The first is a low-density pyrocarbon buffer layer, which allows the diffusion of fission gases and CO(g) from the kernel during fission reactions. The high-density pyrocarbon layer, which retains fission gases, is the second layer. The third layer is SiC, which acts as the main diffusion barrier for non-gaseous fission products. The final layer is another high-density pyrocarbon layer that protects SiC.
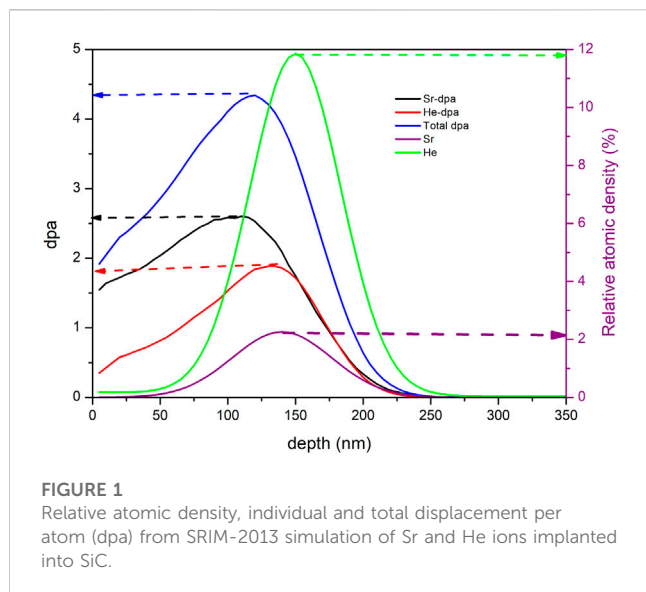
TRISO fuel particles offer an unmatched retention of most radiologically important fission products during normal reactor operation in the temperature range of 900°C–1,300°C (Malherbe et al., 2008), with the exception of strontium (Sr), cesium (Cs), and silver (Ag) (INTERNATIONAL ATOMIC ENERGY AGENCY, 1997). During the normal operation of nuclear reactors, different fission products of different energies are released in the presence of helium. Helium is produced as a byproduct of actinide radioactive decay's alpha decay events and neutron-alpha (n,α) reactions. Helium is insoluble in SiC and forms bubbles when irradiated into SiC with fluences between 5×10^{16} and 1×10^{17} ions/cm² (Gavarini et al., 2020; Liu et al., 2022). The formation of bubbles in SiC results in surface swelling, blistering, and exfoliation (Butterworth, 1989; Grisolia et al., 2000; Zhang et al., 2003; Hinks et al., 2011; Linez et al., 2013; Barcz et al., 2014; Li et al., 2014; Terrani et al., 2014; Li et al., 2015; Linez et al., 2015; Chen et al., 2016; Sun et al., 2018; Daghbouj et al., 2020; Gavarini et al., 2020; Zhang et al., 2021; Clay et al., 2022; Li et al., 2022; Liu et al., 2022; Mokgadi et al., 2022), which affect the structural integrity of SiC as the main barrier to FPs. Thus, it is crucial to study the microstructure of SiC due to the presence of FPs and He and its effect on the migration behaviour of fission products in SiC.

The release of Sr into the environment is a cause for concern. This is because its radioactive isotope, Sr-90, can be absorbed by the body in a similar manner as calcium. This can cause cancer of the bones and teeth. It is therefore important to understand the migration behaviour and mechanisms of Sr in SiC to improve its retention. Thus, some studies have been undertaken to understand the migration behaviour of Sr in SiC in the absence of He (Friedland et al., 2012; Friedland et al., 2013; Dwaraknath and Was, 2016; Abdelbagi et al., 2019; Hlatshwayo et al., 2020). Quite recently, some studies have been undertaken on the effect of helium on the migration behaviour of metallic fission products, viz. silver (Ag), magnesium (Mg), iron (Fe), and strontium (Sr). In the Ag study (Hlatshwayo et al., 2021), no Ag migration was observed in the Ag individually implanted SiC sample after annealing at 1,100°C for 5 h, while migration of Ag towards the bulk and surface was observed in the He and Ag co-implanted SiC after annealing at the same temperature. Hence, He-bubbles enhanced the migration of implanted Ag. However, Mg diffusion was observed to be slower in the He and Mg co-implanted SiC sample annealed at 1,300°C for 20 h compared to the Mg implanted SiC sample annealed at the same conditions (Liu et al., 2021). For Fe in the SiC study (Li et al., 2022), Fe migrated towards the surface in the Fe-implanted SiC

sample annealed at 1,500°C for 2 h, while Fe formed two distinct, spatially separated regions, i.e., close to the surface and trapped around the He-induced defects in the He and Fe co-implanted SiC annealed at 1,500°C for 2 h. In our previous study of Sr implanted into SiC at room temperature in the presence of He (Mokgadi et al., 2022), migration of Sr was enhanced in the He and Sr co-implanted sample annealed at 1,000°C for 5 h. The enhanced migration was accompanied by the trapping of Sr by the He-induced cavities below the surface after annealing at 1,000°C for 5 h. Furthermore, craters as deep as the projected range of the implants were created as a result of He-out-diffusion. So far, in all the reported studies of He and metallic FPs co-implanted with SiC, the implantations were performed at room temperature. However, SiC will be exposed to different irradiations at elevated temperatures during the operation of the nuclear reactor. It is thus crucial to investigate the influence of He and its induced defects on the migration of metallic FPs implanted at elevated temperatures. This work reports on the influence of He on the migration behaviour of Sr implanted at temperatures above the critical amorphization of SiC. 360 keV Sr ions were implanted into polycrystalline SiC at a fluence of 2×10^{16} cm⁻² at 600°C (Sr-SiC). Some of the Sr-implanted SiC samples were then implanted with He ions of 21.5 keV to a fluence of 1×10^{17} cm⁻² at 350°C (Sr + He-SiC). The Sr-SiC and Sr + He-SiC samples were then annealed for 5 h at 1,000°C. The results of the as-implanted and annealed samples were compared to investigate the influence of He.

2 Experimental method

SiC wafers used in this study were purchased from Valley Design Corporation. The as-received wafers were characterized by x-ray diffraction (XRD), Raman spectroscopy, and electron backscatter diffraction (EBSD) (Friedland et al., 2009; Dwaraknath and Was, 2016; Hlatshwayo et al., 2020) and were found to be composed of mostly 3C-SiC with some traces of 6H-SiC. The wafers were then implanted with 360 keV strontium (Sr) ions to a fluence of 2×10^{16} cm⁻² at 600°C (Sr-SiC) under a vacuum of 1×10^{-5} Pa. The Sr implantation was performed at the Friedrich-Schiller-University in Jena, Germany. Some of the Sr implanted wafers were then implanted with Helium (He) ions of energy 21.5 keV at 350°C to a fluence of 1×10^{17} cm⁻² (Sr + He-SiC) at the tandem accelerator mass spectrometry (TAMS) facilities, iThemba LABS, Gauteng, South Africa. In high-temperature fission nuclear reactors, SiC is the main barrier of fission products in the coated TRISO fuel particles will be exposed to different irradiation from different fission products in the presence of He from nuclei decay and transmutation at elevated temperature. He is known to form bubbles in SiC (Gavarini et al., 2020; Liu et al., 2022). These bubbles might compromise SiC as the main barrier to fission products. The energies of Sr and He ions were selected so that they have the nearly the same projected range, thus allowing the investigate of their synergistic effects. To keep with the high-temperature interaction of SiC with fission products during reactor operation, both implantations were performed above (350°C for He and 600°C for Sr) the critical amorphization temperature for SiC (Wendler et al., 1998). The critical temperature at which amorphization does not occur has been

FIGURE 1
Relative atomic density, individual and total displacement per atom (dpa) from SRIM-2013 simulation of Sr and He ions implanted into SiC.

FIGURE 2
Raman spectra of Sr-implanted SiC at 600°C and annealed at 1,000°C for 5 h: **(A)** in the region 600–1,100 cm^{-1}, **(B)** in the region 1,000–2,000 cm^{-1}. Raman spectra of Sr + He-SiC implanted at 600°C and 350°C for Sr and He, respectively, and annealed at 1,000°C for 5 h, **(C)** in the region 600–1,100 cm^{-1}, **(D)** in the region 1,000–2,000 cm^{-1}. In all cases, the virgin spectrum is included for comparison.

reported as about 150°C for Si ions and about 220°C for Xe ions (Snead and Zinkle, 1996). The Sr-SiC and Sr + He-SiC samples were annealed at 1,000°C for 5 h under vacuum (10^{-5} Pa) using a computer-controlled *Webb 77* graphite furnace. The as-implanted and annealed samples were characterized by scanning electron microscopy (SEM), Raman spectroscopy, Rutherford backscattered spectrometry, atomic force microscopy (AFM), and transmission electron microscopy (TEM).

The surface morphological evolution of Sr-SiC and Sr + He-SiC samples was investigated before and after annealing using FEG-SEM (Zeiss Gemini Ultra Plus), Raman spectroscopy (*Witec* alpha 300 *RAS+*), and AFM (Bruker Dimension Icon). The in-lens detector and accelerating voltage of 2 kV were used for FEG-SEM. The 532 nm excitation laser wavelength, 5 mW laser power, and 100 × /0.9 NA objective were used for Raman spectroscopy. The AFM micrographs were analyzed using NanoScope Analysis software over a scan area of 20 µm × 20 µm.The RBS measurements of the Sr-SiC and Sr + He-SiC before and after annealing were performed at the TAMS Laboratory, iThemba LABS, Gauteng, South Africa. The measurements were collected using an alpha particle beam (4 He+) of energy 2.0 MeV, a charge of 0.5 µC, a current of about 500 pA, and a scattering angle of 150°.

TEM lamellae were prepared using a *FEI Helios Nanolab* 650 FIB by focused ion beam (FIB) milling. The samples were thinned to electron transparency using successive Ga ion beam irradiations at 30 keV and 5 keV, followed by final polishing at 2 keV and 500 eV. TEM analysis of the Sr + He-SiC before and after annealing was performed using the *Thermoscientific Talos F200i* field emission transmission electron microscope operating at 200 kV at the Joint Institute for Nuclear Research (JINR), Dubna.

Figure 1 shows the simulated dpa and concentration as a function of the depth of Sr and He implanted into SiC to a fluence of 2×10^{16} and 1×10^{17} cm^{-2}, respectively. The simulations were performed using the stopping and range of ions in matter (SRIM-2013) program (Ziegler et al., 2010). The detailed calculations with full damage cascades were used. The density of 3.21 g cm^{-3} for SiC and the threshold displacement energies, E_d, of
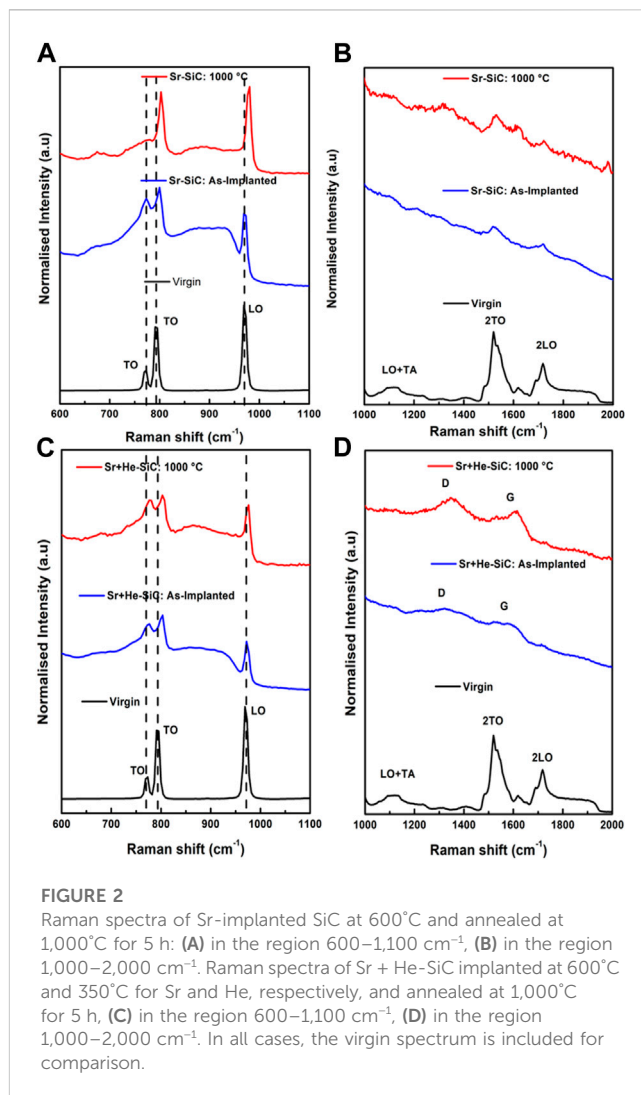
35 and 20 eV for Si and C (Devanathan and Weber, 2000). The implantations resulted in Gaussian profiles with a peak of about 2.26 at% Sr and 12 at% He at a depth of 140 nm and 150 nm, respectively. The simulated maximum dpa of 2.60 and 1.93 at about 110 nm and 130 nm, for Sr and He, respectively, were retained. The calculated total maximum dpa (which is the sum of the maximum individual dpa retained by both ions) at a depth of 110 nm was 4.40 dpa. The simulated results show that Sr and He overlap given the energy choices, which is a requirement in our study of synegic effects.

3 Results

The defects induced in SiC after co-implantation of Sr and He above the critical amorphization temperature of SiC (350°C) were investigated using Raman spectroscopy before and after annealing. Figure 2 shows the Raman spectra of the virgin SiC, Sr-SiC, and Sr + He-SiC samples before and after annealing at 1,000°C for 5 h. All the SiC Raman characteristic peaks of polycrystalline SiC composed of 3C-SiC with some traces of 6H-SiC are present in the virgin spectrum. The transverse optical (TO) peak belonging to
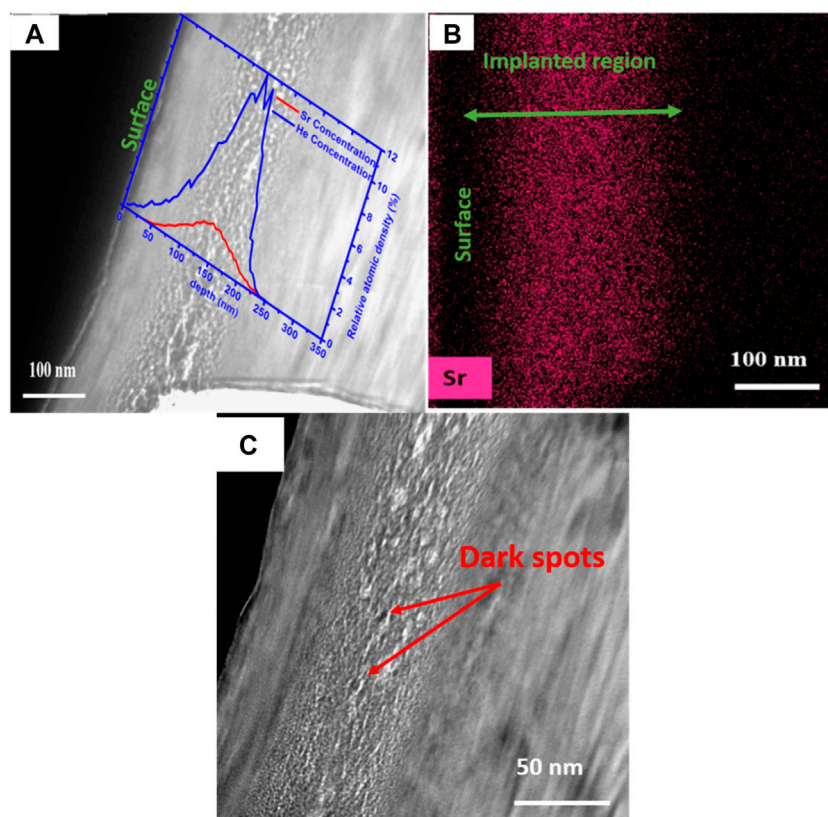
FIGURE 3
A bright field (BF) TEM micrograph of **(A)** Sr + He-SiC and EDX distribution mapping of **(B)** Sr in the as-implanted Sr + He-SiC. The inset in **(A)** is the SRIM simulation of He and Sr depth profiles in SiC. **(C)** The high magnification of the BF TEM micrograph in **(A)** showing dark spots.

the 6H-SiC polytype at 776 cm^{-1} (Madito et al., 2021), the longitudinal optical (LO) peak at 972 cm^{-1}, and the transverse optical (TO) peak at 793 cm^{-1} both belong to the 3C-SiC polytype. These results are in agreement with previous studies (Feng et al., 1988; Nakashima and Harima, 1997; Friedland et al., 2009; Dwaraknath and Was, 2016; Zhang et al., 2019; Hlatshwayo et al., 2020). The second order Raman peaks at 1,115, 1,529, and 1716 cm^{-1} belong to the LO + TA, 2TO, and 2LO modes, respectively (Talwar, 2015).

Sr implantation resulted in a decrease in intensity of the Raman characteristic peaks between 600 and 1,100 cm^{-1}, Figure 2A. The decrease in the peak intensity of the characteristic peaks is due to the accumulation of defects in the structure. This accumulation also resulted in a decrease in the intensity of the second-order peaks in the 1,000–2,000 cm^{-1} regions (Figure 2B). Annealing at 1,000°C for 5 h caused an increase in the intensity of the SiC Raman characteristic peaks. These indicate some limited recovery of SiC structure. There is also a distortion in the TO mode at 776 cm^{-1} after annealing, showing an obliteration of the 6H-SiC polytype traces in the structure. A blue-shift is observed in the TO and LO peaks of the 3C-SiC polytype after implantation and even more after annealing due to local compressive stresses.

Co-implantation of He resulted in a further reduction in the Raman characteristic peaks, indicating further accumulation of defects (Figure 2C). This was further accompanied by the appearance of the D and G peaks (Figure 2D). There is no significant increase in the intensity of the Raman characteristic

peaks after annealing, indicating insignificant annealing of defects. The 6H-SiC TO peak was retained after annealing as compared to the single implanted Sr-SiC sample. The D and G peaks also appear after annealing. Therefore, He implantation retards the recovery process of SiC. A blue-shift of the 3C and 6H-SiC TO peaks is observed before and after annealing, while a slight shift in the LO peak was also observed in the annealed sample.

Figure 3A shows the bright field TEM micrograph of Sr + He-SiC. The highly defective region starts around 75 nm below the surface and extends to a depth of around 320 nm, which makes the highly defective region about 245 nm thick. The white structures parallel to the surface are He-bubbles. The bubbles start at a depth of around 100 nm and extend to about 225 nm below the surface. The SRIM inset in Figure 3A shows the peaks of He and Sr concentrations that correspond with He-bubbles. Dark spots (Figure 3C) are also observed around the He-bubbles, which also correspond to the projected ranges of Sr and He. Figure 3B shows the energy dispersive x-ray (EDX) elemental mapping of Sr. Strontium is evenly distributed in the entire highly defective region of Figure 3A, which extends up to 320 nm below the surface. Figure 3A also shows a rough surface. Helium forms bubbles in SiC at low irradiation temperatures (less than 600°C) (Li et al., 2015; Chen et al., 2016; Daghbouj et al., 2020), as seen in Figure 3A. The formation of these bubbles induces the creation of surface cracks, swelling, and exfoliation, which might be the reason for the surface roughness.
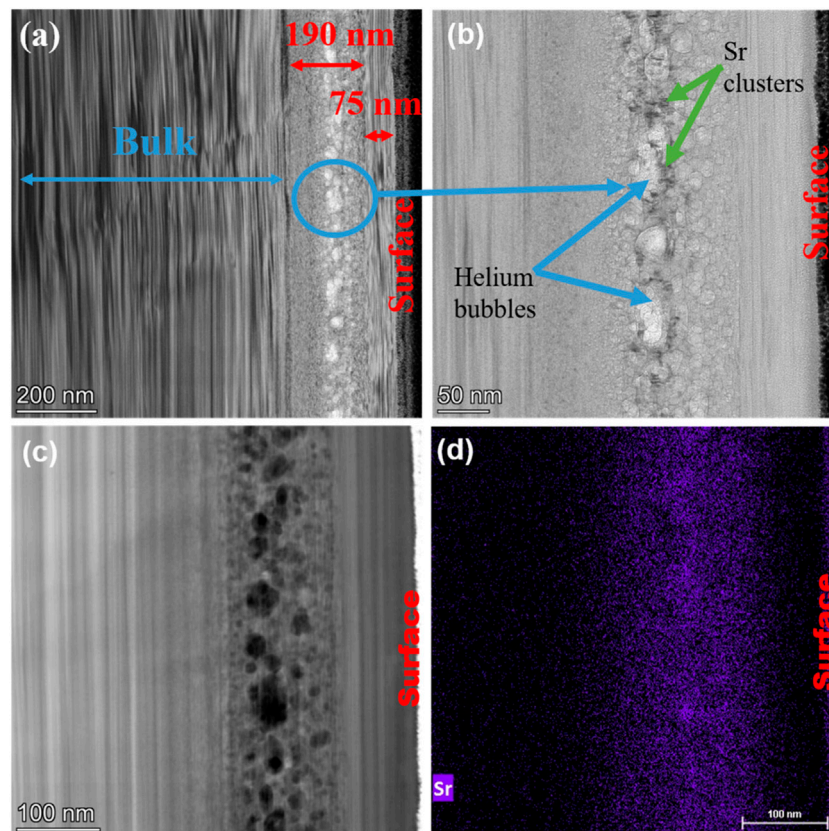
FIGURE 4
Bright field (BF) TEM micrographs of **(A)** Sr + He-SiC annealed at 1,000°C for 5 h, low magnification, and **(B)** high magnification. **(C)** A dark field (DF) TEM micrograph of Sr in annealed Sr + He-SiC, and **(D)** EDX distribution mapping of Sr in annealed Sr + He-SiC.

Figure 4A shows the low magnification bright field TEM micrograph of Sr + He-SiC annealed at 1,000°C. The crystalline region of about 75 nm thickness from the surface to the damage region is still present in the annealed sample, similar to the as-implanted sample. The damage region is approximately 190 nm thick, with helium bubbles located near the maximum concentrations of He and Sr. This is a decrease in the damage region from about 245 nm in the as-implanted sample to 190 nm in the annealed sample. Figure 4B shows the high-magnification BF micrograph showing enlarged He-bubbles after annealing. Annealing also caused the region with bubbles to grow from a thickness of about 125 nm in the as-implanted sample to about 150 nm in the annealed sample. What is also evident from Figure 4B is that the smaller bubbles start forming at the start of the defective region and grow toward the center. Since He-atoms require defects to agglomerate and form bubbles, most defects are retained around the maximum concentration of He and Sr, hence the bigger bubbles around that depth. The He-bubbles absorb the smaller ones as the temperature increases, and that's how they grow in size. The dark structures around the enlarged He-bubbles might be Sr clusters. Figure 4C shows the dark field TEM micrograph; the dark structures, in this case, are He-bubbles, and the white structures around the dark structures, similar to the dark structure in Figure 4B, might be Sr. Figure 4D shows the EDX elemental mapping of Sr. The Sr distribution is fairly even, similar to the

as-implanted Sr + He-SiC sample. However, some Sr-atom clusters are observed around the He-bubbles, which confirms that the dark structures in Figure 4B are Sr-atoms. These Sr-atoms might be trapped by the defect clusters that are near the He-bubbles.

Figure 5 shows the SEM micrographs of Sr-SiC before and after annealing; the pristine SiC micrograph is also included for comparison. The pristine SiC has polishing marks and grain boundaries, while the as-implanted sample still has some polishing marks and some grain boundaries. The slight dissaperance of grain boundaries is due to the sputtering of SiC due to Sr ions during implantation. Annealing at 1,000°C also resulted in the appearance of polishing marks and some grain boundaries due to recrystallization.

Figure 6 shows the SEM and AFM micrographs of the Sr + He-SiC before and after annealing. The surface roughness and irregularities seen in Figure 3 above are confirmed by the formation of the irregular structures in Figures 6A, B. The co-implantation of He resulted in the formation of irregular structures on the surface that were not observed in the as-implanted Sr-SiC sample. The structures grew in size after annealing the Sr + He-SiC sample at 1,000°C. The structures on the surface might be blisters and craters, which are helium-induced defects. To fully differentiate between these helium-induced defects, AFM was performed. The bright structures in Figures 6C, D are blisters, since high structures appear bright and shallow structures appear dark in AFM. Therefore, the dark structures are craters/holes.
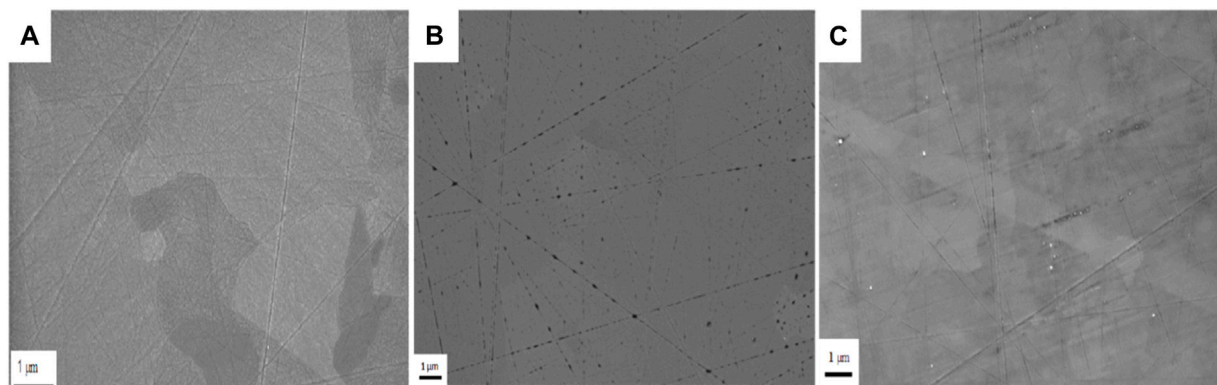
FIGURE 5
SEM micrographs of **(A)** pristine SiC, **(B)** as-implanted Sr at 600°C and **(C)** Sr-implanted SiC then annealed at 1,000°C for 5 h.
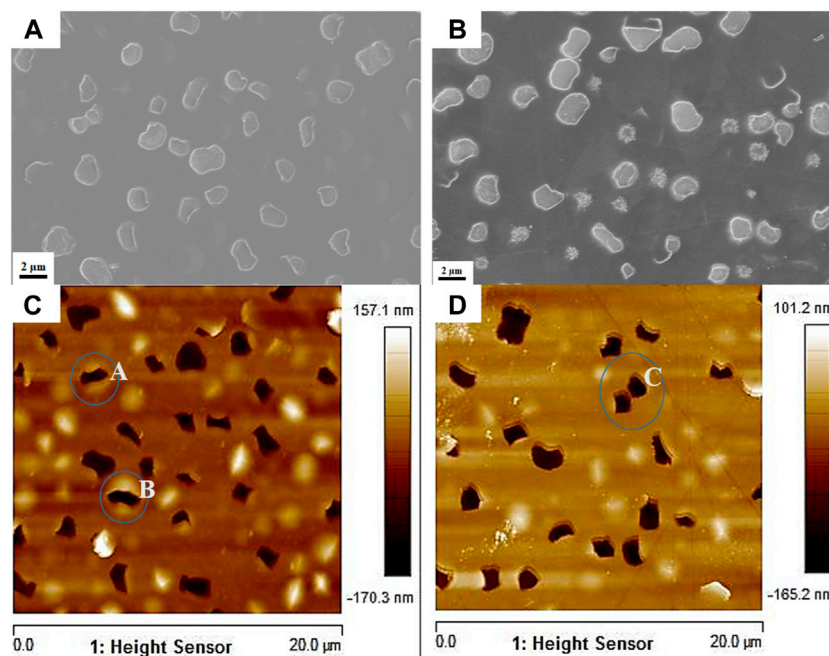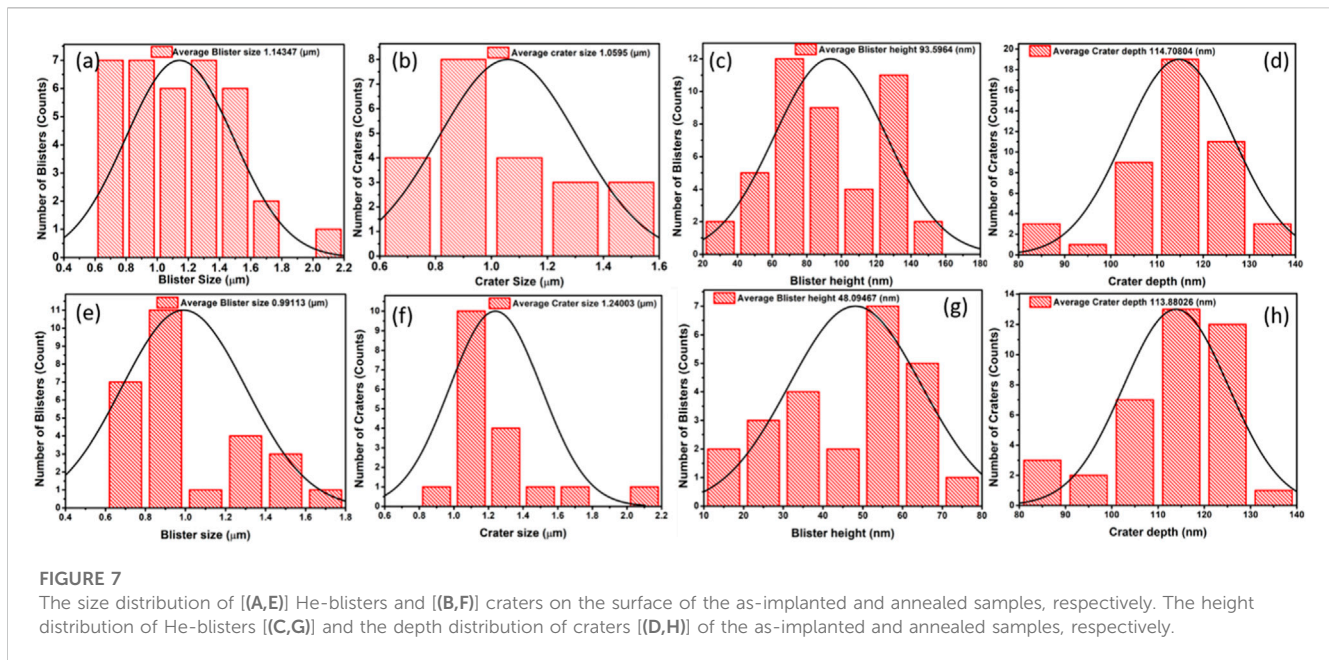

FIGURE 6
SEM micrographs of **(A)** Sr + He-SiC as-implanted sample and **(B)** Sr + He-SiC annealed sample at 1,000°C for 5 h, and their respective AFM micrographs [**(C,D)**]. Circles A and B in **(C)** show craters that form within blisters, while Circle C in **(D)** shows two neighbouring craters that would eventually merge.

Qualitatively, it is observed from the AFM micrographs that the number of blisters and craters varies between the as-implanted and annealed samples. To quantify this, the size, height, and depth statistics of the He-blisters and craters formed on the surface of the AFM micrographs of as-implanted and annealed samples were analyzed using the ImageJ software and are displayed in Figure 7. The size of the blisters in the as-implanted sample varies from 0.6 to 2.2 µm, while in the annealed sample they range from 0.6 to 1.8 µm. The mean blister size was measured to be about 1.14 ± 0.35 µm and 0.99 ± 0.31 µm for the as-implanted and annealed samples, respectively. The number density of the He-blisters were calculated to be 9×10^6 cm^{-2} and 2.5×10^6 cm^{-2}, for the as-implanted and

annealed samples, respectively. The height of the blisters in the as-implanted sample (Figures 7A, E) varies from 20 to 160 nm, and in the annealed sample, from 10 to 80 nm in Figures 7C, G, respectively. The mean blister heights were found to be about 93.60 ± 32.27 nm and 46.09 ± 16.61 nm, for the as-implanted and annealed samples, respectively.

Figures 7B, F show the measured size of the craters for the as-implanted and annealed samples, respectively. The sizes varied from 0.6 to 1.4 µm in the as-implanted sample and 0.8–2.2 µm in the annealed sample. The mean diameter of the craters was found to be about 1.06 ± 0.25 µm for the as-implanted sample and 1.24 ± 0.27 µm for the annealed sample. The number density of the

FIGURE 7
The size distribution of [(A,E)] He-blisters and [(B,F)] craters on the surface of the as-implanted and annealed samples, respectively. The height distribution of He-blisters [(C,G)] and the depth distribution of craters [(D,H)] of the as-implanted and annealed samples, respectively.

craters was calculated to be 7.25×10^6 cm^{-2} for the as-implanted sample and 4.5×10^6 cm^{-2} for the annealed sample. Figures 7D, H show the depth measurements of the craters before and after annealing, respectively. The depth of the craters ranges from 80 to 140 nm for both the as-implanted and annealed samples. The mean depth of the craters was also calculated and was found to be similar for the as-implanted (114.71 ± 11.74 nm) and the annealed samples (113.88 ± 11.36 nm). Some of the blisters in the as-implanted sample, circled A and B in Figure 6C, do not fully exfoliate, hence, the crater forms within the blister. When these blisters exfoliate after annealing, they increase the size of the crater. Thus, the increase in the mean crater size after annealing. This increase in the mean size is also due to the exfoliation of blisters in neighbouring craters and the joining of two craters to form one crater, as indicated by circle C in Figure 6D. The joining of neighbouring craters decreases their number density. The mean depth of the craters is similar for both the as-implanted and annealed samples. This is because the He-bubbles start forming around the maximum concentration of He and Sr, and if they grow big enough, they form blisters on the surface and eventually exfoliate that form craters.

The migration of Sr in Sr-SiC and Sr + He-SiC samples before and after annealing at 1,000°C for 5 h was monitored using RBS. Figures 8A, B shows the RBS spectra of the as-implanted Sr-SiC and Sr + He-SiC (a) and (b), the Sr-SiC sample before and after annealing (c) and (d), and the Sr + He-SiC sample before and after annealing (e) and (f). The surface positions of elements are indicated by arrows in Figure 8. He co-implantation in Sr pre-implanted SiC resulted in slight Sr migration towards the bulk and the surface, with the migration towards the bulk being more pronounced. The migration of Sr in the co-implanted sample is due to the formation of He bubbles, blisters, and craters on the SiC surface, as seen in Figure 6. As mentioned before, the formation of He-bubbles requires vacancies that are dominant around the projected range of Sr. As a result, larger bubbles are formed around the projected range. For a bubble to grow,

it must capture more vacancies from the surroundings, which results in the Sr atoms moving in the opposite direction, thus migrating towards the bulk and the surface. The more pronounced migration could be explained by the fact that there were fewer vacancies available towards the surface from the projected range peak position of Sr compared to the region towards the bulk/crystalline SiC. However, since the surface is a reference during RBS analysis, the rough surface in the Sr + He-SiC sample might also cause the Sr profile to appear broader compared to the Sr profile of the Sr-SiC samples (which have a relatively flat surface).

Annealing the Sr-SiC sample at 1,000°C for 5 h caused no changes in the RBS spectrum compared with the as-implanted spectrum (Figures 8C, D), indicating no detectable migration of Sr in the annealed sample. After 5 h of annealing the Sr + He-SiC sample at 1,000°C, the Sr profile shifted towards lower channel numbers, indicating Sr migration to the bulk (Figures 8E, F). This resulted in a Sr peak forming a double peak with a minimum around channel number 276. Similar formation of double Sr peaks indicating migration and trapping of implanted Sr was reported for Sr and He co-implanted into SiC at RT after annealing at 1,000°C for 5 h (Mokgadi et al., 2022). Unlike in the previous study (Mokgadi et al., 2022), where the Sr atoms migrated in both directions in the annealed RT-implanted Sr + He-SiC samples, the Sr atoms in this case migrated only towards the bulk. This might indicate the role of defects retained by pre-implanted Sr ions, i.e., implantation at RT amorphized SiC while implantation at 600°C retained the crystallinity of SiC with some defects.

4 Discussion

The variation in the size, number density, and height of the blisters before and after annealing point to the crucial relationship between He-blister formation and local defects in the structure. The local defects trap He-atoms, and the high
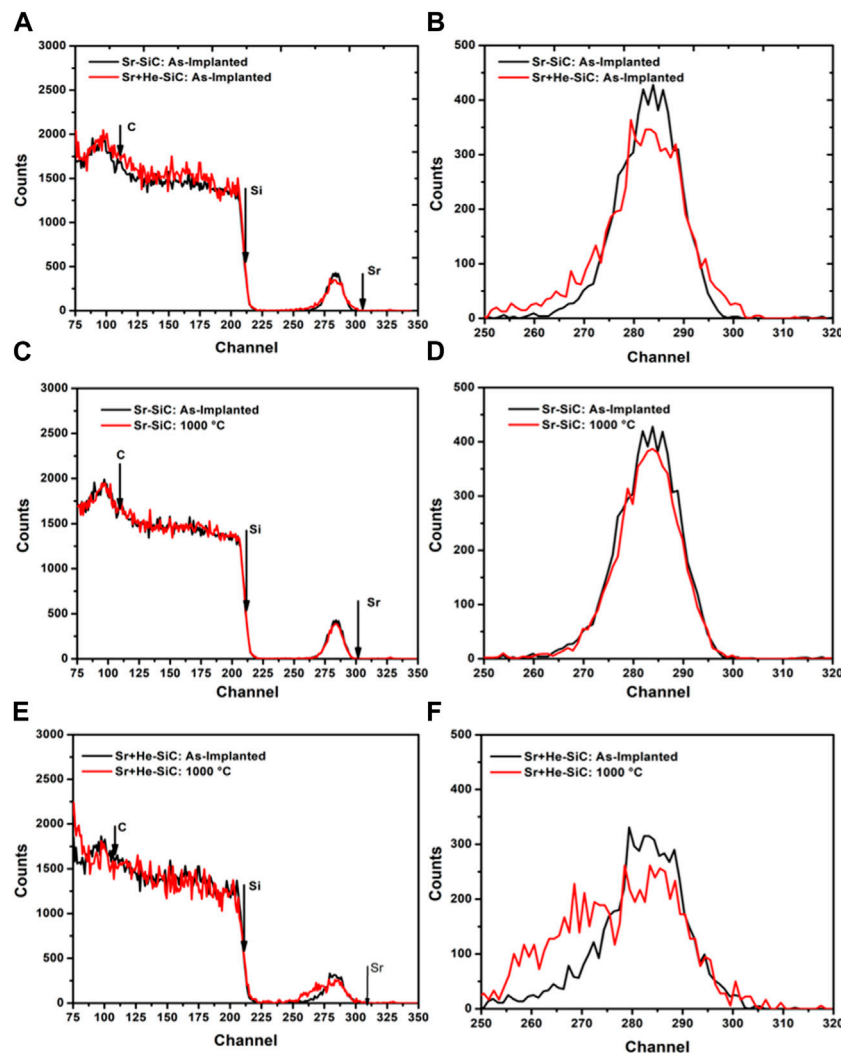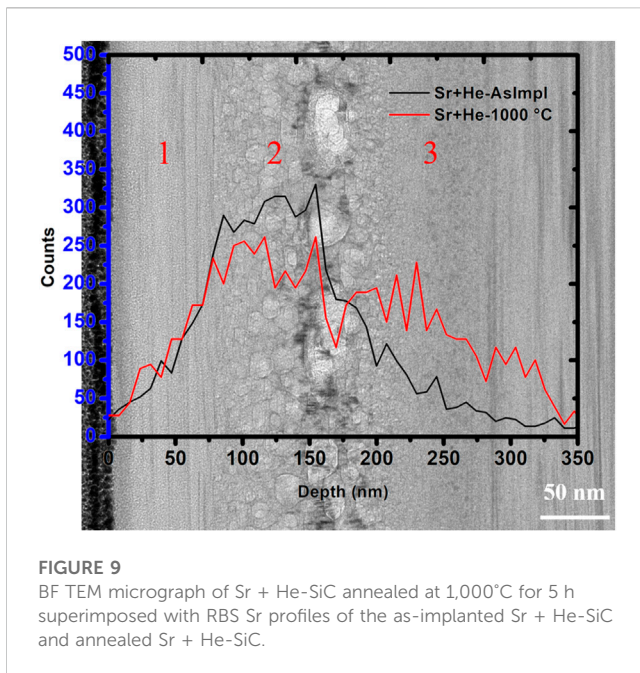
FIGURE 8
RBS spectra of **(A)** as-implanted Sr-SiC and Sr + He-SiC, **(C)** Sr-SiC as-implanted and annealed at 1,000°C, and **(E)** Sr + He-SiC as-implanted and annealed at 1,000°C. **(B)**, **(D)**, and **(F)** show the respective zoomed-in profiles of the RBS spectra.

temperature gives these trapped He-atoms enough energy to move and coalesce to form bigger bubbles below the surface. The blisters form as a result of the growth of the bubbles as they accumulate more He-atoms. The pressure within the bubbles will start to push against the surface. If this accumulation continues, the size and height of the blisters will increase, depending on the surface energy and fracture toughness of SiC. The He-atoms will then exert pressure on the blister walls, causing the stress intensity factor at the tip, K_I, to be higher than the fracture toughness of SiC (Reboh et al., 2011; Daghbouj et al., 2019; Daghbouj et al., 2021). This will lead to blister exfoliation and the formation of craters as the gas diffuses. As a result, the average crater size may provide the average size for the blister to exfoliate, which is approximately 1.06 µm. The size, height, and number density of the blisters decreased after annealing; this is because the bigger blisters in the as-implanted sample will be the first to exfoliate and form craters. New blisters will start to form, but because most of the He-atoms have out-diffused during the

implantation process and the number of defects has decreased, they will appear small and short.

The formed craters contribute to Sr loss, and their density correlates with the lost implanted species. Exfoliating blisters also fragment the host, releasing host material and neighboring substances, including Sr near He-bubbles. Thus, roughly 6.40% of craters cover the as-implanted surface, while about 5.50% occupy the annealed sample's surface. This minor disparity indicates limited migration towards the surface in both as-implanted and annealed samples. Figure 9 shows the BF TEM micrograph superimposed with the RBS depth profile of Sr in as-implanted Sr + He-SiC and annealed Sr + He-SiC samples. The RBS spectra in channel number were converted using energy loss factor data from Ziegler (Ziegler et al., 2010) and the density of perfect SiC crystals (3.21 g cm^{-3}). Based on the results presented in Figure 9. Sr atoms are located in three regions, i.e., in the first less defective region about 75 nm from the surface (region 1), in the highly defective region with He bubbles (region 2), and in the

FIGURE 9
BF TEM micrograph of Sr + He-SiC annealed at 1,000°C for 5 h superimposed with RBS Sr profiles of the as-implanted Sr + He-SiC and annealed Sr + He-SiC.

region between the substrate and the highly defective region with bubbles (region 3). Annealing of the Sr + He-SiC sample resulted in the migration of Sr towards the bulk, i.e., in the third region. Comparing the simulated results in Figure 1 with the TEM results, it is quite clear that the highly defective region corresponds to the region with high dpa values which is also a region with most of the implanted ions. For bubbles to grow in the second region, they will have to capture vacancies/interstitials in region 3, which will also allow the Sr atoms to move in the opposite direction of the vacancies/interstitials, i.e., vacancy diffusion or interstitial diffusion. Hence, the growth of bubbles accompanied by Sr migration towards the bulk is due to the combination of vacancy diffusion and interstitial diffusion driven by strain fields. It is known that the interstitials start to diffuse from low strained area (in region 3 in this study) to the highly strained area (in region 2 in this study) (Hlatshwayo et al., 2021).

5 Summary

The influence of the He-induced defects (blisters, He-bubbles, cavities, and craters) on the migration behaviour of Sr implanted at temperatures above the critical amorphization of SiC and annealing was investigated. Sr ions were first implanted into polycrystalline SiC at 600°C (Sr-SiC), and then He ions were implanted in the same SiC at 350°C (Sr + He-SiC). Both Sr-SiC and Sr + He-SiC were annealed for 5 h at 1,000°C. Implantation of Sr resulted in SiC with defects, while co-implantation of He resulted in three implanted regions: the crystalline layer (closer to the surface), the defective layer with He bubbles, and the defective layer close to the unaffected SiC or substrate. The second region contained both He and Sr peaks. Blisters and craters were also observed in the as-implanted Sr + He-SiC samples. Annealing caused He-bubbles to grow in size. The

growth of He bubbles was due to He bubbles capturing more vacancies during annealing. The blister number density and blister height reduced significantly after annealing due to the recovery of radiation-induced defects, while the size of the craters increased significantly after annealing due to the merging of neighbouring craters. No diffusion was observed in the Sr-SiC annealed sample. However, annealing the Sr + He-SiC sample caused the migration of Sr toward the bulk. The migration was found to be due to vacancy diffusion driven by strain fields. Therefore, vacancy diffusion might be playing a role in the migration of Sr in the TRISO particle.

Data availability statement

Data will be made available on request.

Author contributions

TM: Conceptualization, Methodology, Investigation, Formal analysis, Writing—original draft, Preparation, Visualization. ZA: Writing—review & editing, Validation. MM: Investigation. EN: Writing—review & editing, Validation. MM: Data curation, Visualization, Investigation. PM Funding acquisition, Resources, Validation. AS: Investigation, Validation. VS: Validation, Resources. JM: Conceptualization, Methodology, Validation, Resources. TH: Conceptualization, Methodology, Validation, Resources, Supervision, Project administration, Funding acquisition, Writing—review & editing.

Conflict of interest

Authors MM and PM were employed by Mintek.

The remaining authors declare that the research was conducted in the absence of any commercial or financial relationships that could be construed as a potential conflict of interest.

Publisher's note

All claims expressed in this article are solely those of the authors and do not necessarily represent those of their affiliated organizations, or those of the publisher, the editors and the reviewers. Any product that may be evaluated in this article, or claim that may be made by its manufacturer, is not guaranteed or endorsed by the publisher.

References

Abdelbagi, H. A. A., Skuratov, V. A., Motloung, S. V., Njoroge, E. G., Mlambo, M., Hlatshwayo, T. T., et al. (2019). Effect of swift heavy ions irradiation on the migration behavior of strontium implanted into polycrystalline SiC. *Nucl. Instrum. Methods Phys. Res. B* 451, 113–121. doi:10.1016/j.nimb.2019.05.039

Avincola, V. A., Grosse, M., Stegmaier, U., Steinbrueck, M., and Seifert, H. J. (2015). Oxidation at high temperatures in steam atmosphere and quench of silicon carbide composites for nuclear application. *Nucl. Eng. Des.* 295, 468–478. doi:10.1016/j.nucengdes.2015.10.002

Barcz, A., Kozubal, M., Jakieła, R., Ratajczak, J., Dyczewski, J., Gołaszewska, K., et al. (2014). Diffusion and impurity segregation in hydrogen-implanted silicon carbide. *J. Appl. Phys.* 115 (22), 223710. doi:10.1063/1.4882996

Butterworth, G. J. (1989). Low activation structural materials for fusion. *Fusion Eng. Des.* 11 (1-2), 231–244. doi:10.1016/0920-3796(89)90021-5

Carter, C. H., Jr, Davis, R. F., and Bentley, J. (1984). Kinetics and mechanisms of high-temperature creep in silicon carbide: II, chemically vapor deposited. *J. Am. Ceram. Soc.* 67 (11), 732–740. doi:10.1111/j.1151-2916.1984.tb19510.x

Chen, C. H., Zhang, Y., Wang, Y., Crespillo, M. L., Fontana, C. L., Graham, J. T., et al. (2016). Dose dependence of helium bubble formation in nano-engineered SiC at 700°C. *J. Nucl. Mater.* 472, 153–160. doi:10.1016/j.jnucmat.2016.01.029

Clay, B. T., Donnelly, S. E., and Greaves, G. (2022). Observations of He platelets during He ion irradiation in 3C SiC. *J. Nucl. Mater* 559, 153426. doi:10.1016/j.jnucmat.2021.153426

Daghbouj, N., Li, B. S., Callisti, M., Sen, H. S., Lin, J., Ou, X., et al. (2020). The structural evolution of light-ion implanted 6H-SiC single crystal: comparison of the effect of helium and hydrogen. *Acta Mater* 188, 609–622. doi:10.1016/j.actamat.2020.02.046

Daghbouj, N., Li, B. S., Karlik, M., and Declemy, A. J. A. S. S. (2019). 6H-SiC blistering efficiency as a function of the hydrogen implantation fluence. *Appl. Surf. Sci.* 466, 141–150. doi:10.1016/j.apsusc.2018.10.005

Daghbouj, N., Lin, J., Sen, H. S., Callisti, M., Li, B., Karlik, M., et al. (2021). Blister formation in He-H co-implanted InP: a comprehensive atomistic study. *Appl. Surf. Sci.* 552, 149426. doi:10.1016/j.apsusc.2021.149426

Devanathan, R., and Weber, W. J. (2000). Displacement energy surface in 3C and 6H SiC. *J. Nucl. Mater.* 278 (2-3), 258–265. doi:10.1016/s0022-3115(99)00266-4

Dwaraknath, S. S., and Was, G. S. (2016). The diffusion of cesium, strontium, and europium in silicon carbide. *J. Nucl. Mater.* 476, 155–167. doi:10.1016/j.jnucmat.2016.04.034

Feng, Z. C., Choyke, W. J., and Powell, J. A. (1988). Raman determination of layer stresses and strains for heterostructures and its application to the cubic SiC/Si system. *J. Appl. Phys.* 64 (12), 6827–6835. doi:10.1063/1.341997

Friedland, E., Hlatshwayo, T., and Van der Berg, N. (2013). Influence of radiation damage on diffusion of fission products in silicon carbide. *Phys. status solidi C.* 10 (2), 208–215. doi:10.1002/pssc.201200457

Friedland, E., Malherbe, J. B., Van der Berg, N. G., Hlatshwayo, T., Botha, A. J., Wendler, E., et al. (2009). Study of silver diffusion in silicon carbide. *J. Nucl. Mater.* 389 (2), 326–331. doi:10.1016/j.jnucmat.2009.02.022

Friedland, E., van der Berg, N. G., Malherbe, J. B., Wendler, E., and Wesch, W. (2012). Influence of radiation damage on strontium and iodine diffusion in silicon carbide. *J. Nucl. Mater.* 425 (1-3), 205–210. doi:10.1016/j.jnucmat.2011.10.032

Gavarini, S., Baillet, J., Millard-Pinard, N., Garnier, V., Peaucelle, C., Jaurand, X., et al. (2020). Effects of helium irradiation on fine grained β-SiC synthesized by spark plasma sintering. *J. Eur. Ceram. Soc.* 40 (1), 1–11. doi:10.1016/j.jeurceramsoc.2019.09.018

George, N. M., Terrani, K., Powers, J., Worrall, A., and Maldonado, I. (2015). Neutronic analysis of candidate accident-tolerant cladding concepts in pressurized water reactors. *Ann. Nucl. Energy* 75, 703–712. doi:10.1016/j.anucene.2014.09.005

Grisolia, J., Cristiano, F., De Mauduit, B., Assayag, G. B., Letertre, F., Aspar, B., et al. (2000). Kinetic aspects of the growth of hydrogen induced platelets in SiC. *J. Appl. Phys.* 87 (12), 8415–8419. doi:10.1063/1.373556

Hinks, J. A., Van Den Berg, J. A., and Donnelly, S. E. (2011). MIAMI: microscope and ion accelerator for materials investigations. *J. Vac. Sci. Technol. A Vac. Surf. Films* 29 (2), 021003. doi:10.1116/1.3543707

Hlatshwayo, T. T., Maepa, C. E., Msimanga, M., Mlambo, M., Njoroge, E. G., Skuratov, V. A., et al. (2021). Helium assisted migration of silver implanted into SiC. *Vacuum* 183, 109865. doi:10.1016/j.vacuum.2020.109865

Hlatshwayo, T. T., Mtshonisi, N., Njoroge, E. G., Mlambo, M., Msimanga, M., Skuratov, V. A., et al. (2020). Effects of Ag and Sr dual ions implanted into SiC. *Nucl. Instrum. Methods Phys. Res. B* 472, 7–13. doi:10.1016/j.nimb.2020.03.035

INTERNATIONAL ATOMIC ENERGY AGENCY (1997). *Fuel performance and fission product behaviour in gas-cooled reactors*. Vienna: IAEA-TECDOC-978, IAEA. Available from: http://www-pub.iaea.org/books/IAEABooks/5633/Fuel-Performance-and-Fission-ProductBehaviour-in-GasCooled-Reactors.

Katoh, Y., Kohyama, A., Nozawa, T., and Sato, M. (2004). SiC/SiC composites through transient eutectic-phase route for fusion applications. *J. Nucl. Mater.* 329, 587–591. doi:10.1016/j.jnucmat.2004.04.157

Katoh, Y., Snead, L. L., Henager, C. H., Jr, Hasegawa, A., Kohyama, A., Riccardi, B., et al. (2007). Current status and critical issues for development of SiC composites for fusion applications. *J. Nucl. Mater.* 367, 659–671. doi:10.1016/j.jnucmat.2007.03.032

Li, B. S., Du, Y. Y., and Wang, Z. G. (2015). Recrystallization of He-ion implanted 6H-SiC upon annealing. *Nucl. Instrum. Methods Phys. Res. B* 345, 53–57. doi:10.1016/j.nimb.2014.12.049

Li, B. S., Sen, H. S., Daghbouj, N., AlMotasem, A. T., Lorinčík, J., Karlik, M., et al. (2022). Thermal behavior of iron in 6H-SiC: influence of He-induced defects. *Scr. Mater.* 218 (1), 114805. doi:10.1016/j.scriptamat.2022.114805

Li, B. S., Wang, Z. G., Zhang, C. H., Wei, K. F., Yao, C. F., Sun, J. R., et al. (2014). Evolution of strain and mechanical properties upon annealing in He-implanted 6H-SiC. *J. Nucl. Mater.* 455 (1-3), 116–121. doi:10.1016/j.jnucmat.2014.05.028

Linez, F., Garrido, F., Erramli, H., Sauvage, T., Courtois, B., Desgardin, P., et al. (2015). Experimental location of helium atoms in 6H–SiC crystal lattice after implantation and after annealing at 400°C. *J. Nucl. Mater.* 459, 62–69. doi:10.1016/j.jnucmat.2014.12.118

Linez, F., Gilabert, E., Debelle, A., Desgardin, P., and Barthe, M. F. (2013). Helium interaction with vacancy-type defects created in silicon carbide single crystal. *J. Nucl. Mater.* 436 (1-3), 150–157. doi:10.1016/j.jnucmat.2013.01.288

Liu, M., Gong, H., Liu, W., Liu, R., and Cao, J. (2021). Effects of He on the recrystallization and Mg diffusion in Mg ion implanted CVD-SiC. *J. Nucl. Mater.* 545, 152747. doi:10.1016/j.jnucmat.2020.152747

Liu, M., Yan, Y., Zhu, Z., Liu, R., Ye, L., Zhou, H., et al. (2022). Microstructural evolution, swelling and hardening of CVD-SiC induced by He ions irradiation at 650°C. *Ceram. Int.* 49, 1880–1887. doi:10.1016/j.ceramint.2022.09.152

Madito, M. J., Hlatshwayo, T. T., and Mtshali, C. B. (2021). Chemical disorder of a-SiC layer induced in 6H-SiC by Cs and I ions co-implantation: Raman spectroscopy analysis. *Appl. Surf. Sci.* 538, 148099. doi:10.1016/j.apsusc.2020.148099

Malherbe, J. B., Friedland, E., and Van Der Berg, N. G. (2008). Ion beam analysis of materials in the PBMR reactor. *Nucl. Instrum. Methods Phys. Res. B* 266 (8), 1373–1377. doi:10.1016/j.nimb.2007.10.046

Mokgadi, T., Abdalla, Z., Abdelbagi, H., Msimanga, M., Maepa, C., Skuratov, V., et al. (2022). Helium and strontium co-implantation into SiC at room temperature and isochronal annealing: structural evolution of SiC and migration behaviour of strontium. *Mater. Chem. Phys.* 294, 126998. doi:10.1016/j.matchemphys.2022.126998

Nakashima, S. I., and Harima, H. (1997). Raman investigation of SiC polytypes. *Phys. Status Solidi* 162 (1), 39–64. doi:10.1002/1521-396x(199707)162:1<39::aid-pssa39>3.0.co;2-l;2-L

Pint, B. A., Terrani, K. A., Brady, M. P., Cheng, T., and Keiser, J. R. (2013). High temperature oxidation of fuel cladding candidate materials in steam–hydrogen environments. *J. Nucl. Mater.* 440 (1-3), 420–427. doi:10.1016/j.jnucmat.2013.05.047

Reboh, S., De Mattos, A. A. D., Schaurich, F., Fichtner, P. F. P., Beaufort, M. F., and Barbot, J. F. (2011). The mechanisms of surface exfoliation in H and He implanted Si crystals. *Scr. Mater.* 65 (12), 1045–1048. doi:10.1016/j.scriptamat.2011.09.012

Snead, L. L., Nozawa, T., Ferraris, M., Katoh, Y., Shinavski, R., and Sawan, M. (2011). Silicon carbide composites as fusion power reactor structural materials. *J. Nucl. Mater.* 417 (1-3), 330–339. doi:10.1016/j.jnucmat.2011.03.005

Snead, L. L., Nozawa, T., Katoh, Y., Byun, T. S., Kondo, S., and Petti, D. A. (2007). Handbook of SiC properties for fuel performance modeling. *J. Nucl. Mater.* 371 (1-3), 329–377. doi:10.1016/j.jnucmat.2007.05.016

Snead, L. L., and Zinkle, S. J. (1996). Threshold irradiation dose for amorphization of silicon carbide. *MRS Online Proc. Libr. Opl.* 439, 595. doi:10.1557/PROC-439-595

Sun, J., Li, B. S., You, Y. W., Hou, J., Xu, Y., Liu, C. S., et al. (2018). The stability of vacancy clusters and their effect on helium behaviors in 3C-SiC. *J. Nucl. Mater.* 503, 271–278. doi:10.1016/j.jnucmat.2018.03.010

Talwar, D. N. (2015). Probing optical, phonon, thermal and defect properties of 3C-SiC/Si (001). *Diam. Relat. Mater.* 52, 1–10. doi:10.1016/j.diamond.2014.11.011

Terrani, K. A., Pint, B. A., Parish, C. M., Silva, C. M., Snead, L. L., and Katoh, Y. (2014). Silicon carbide oxidation in steam up to 2 MPa. *J. Am. Ceram. Soc.* 97 (8), 2331–2352. doi:10.1111/jace.13094

Wendler, E., Heft, A., and Wesch, W. (1998). Ion-beam induced damage and annealing behaviour in SiC. *Nucl. Instrum. Methods Phys. Res. B* 141 (1-4), 105–117. doi:10.1016/S0168-583X(98)00083-4

Zhang, C. H., Donnelly, S. E., Vishnyakov, V. M., and Evans, J. H. (2003). Dose dependence of formation of nanoscale cavities in helium-implanted 4H–SiC. *J. Appl. Phys.* 94 (9), 6017–6022. doi:10.1063/1.1611630

Zhang, L., Jiang, W., Pan, C., Fadanelli, R. C., Ai, W., Chen, L., et al. (2019). Raman study of amorphization in nanocrystalline 3C–SiC irradiated with C+ and He+ ions. *J. Raman Spectrosc.* 50 (8), 1197–1204. doi:10.1002/jrs.5631

Zhang, T., He, X., Chen, L., Li, J., Liao, Q., Xu, S., et al. (2021). The effect of cavities on recrystallization growth of high-fluence He implanted-SiC. *Nucl. Instrum. Methods Phys. Res. B Beam Interact. Mater. At.* 509, 68–72. doi:10.1016/j.nimb.2021.08.012

Ziegler, J. F., Ziegler, M. D., and Biersack, J. P. (2010). SRIM–The stopping and range of ions in matter. *Nucl. Instrum. Methods Phys. Res. B* 268 (11-12), 1818–1823. doi:10.1016/j.nimb.2010.02.091